Journal Name

ARTICLE

Magnetron-sputtered copper nanoparticles: lost in gas aggregation and found by *in situ* X-ray scattering

Received 00th January 20xx,
Accepted 00th January 20xx

DOI: 10.1039/x0xx00000x

www.rsc.org/

Jaroslav Kousal,[a] Artem Shelemin,[a] Matthias Schwartzkopf,[b] Oleksandr Polonskyi,[c] Jan Hanuš,[a] Pavel Solař,[a] Mykhailo Vaidulych,[a] Daniil Nikitin,[a] Pavel Pleskunov,[a] Zdeněk Krtouš,[a] Thomas Strunskus,[c] Franz Faupel,[c] Stephan V. Roth,[b, d] Hynek Biederman,[a] and Andrei Choukourov*[a]

Magnetron discharge in a cold buffer gas represents a liquid-free approach to the synthesis of metal nanoparticles (NPs) with tailored structure, chemical composition and size. Despite a large number of metal NPs that were successfully produced by this method, the knowledge of the mechanisms of their nucleation and growth in the discharge is still limited, mainly because of the lack of *in situ* experimental data. In this work, we present the results of *in situ* Small Angle X-ray Scattering measurements performed in the vicinity of a Cu magnetron target with Ar used as a buffer gas. Condensation of atomic metal vapours is found to occur mainly at several mm distance from the target plane. The NPs are found to be captured preferentially within a region circumscribed by the magnetron plasma ring. In this capture zone, the NPs grow to the size of 90 nm whereas smaller ones sized 10-20 nm may escape and constitute a NP beam. Time-resolved measurements of the discharge indicate that the electrostatic force acting on the charged NPs may be largely responsible for their capturing nearby the magnetron.

Introduction

Gas-phase synthesis of metal nanoparticles (NPs) has been attracting scientific interest for a long time. Starting from the pioneering work by Pfund,[1] a number of experimental approaches have been suggested through the following decades. Though diverse, they all share a common feature: metal should be transferred into atomic vapours in a certain manner and then the conditions of supersaturation should be created to trigger the spontaneous nucleation and formation of metal NPs. In the 1990s, magnetron sputtering was found to be a particularly useful tool for 'vaporizing' metals, especially when performed in the configuration of a gas aggregation cluster source (GAS).[2,3] In this configuration, a magnetron is installed in a separate vacuum chamber and metal is sputtered into a flow of a buffer gas. The pressure and the flow of the buffer gas are tuned to force the formation of NPs and to transport them away from the discharge zone. Thus-produced NPs are typically extracted from the GAS *via* a small orifice into another vacuum chamber where their analysis and/or deposition onto solid substrates can be performed. The method has acquired particular popularity as is evidenced by an increasing number of papers that have been published in recent years. Single-metal,[4–15] alloyed[16–26] and heterostructured NPs[27–40] have been successfully synthesized. However, detailed information about the process kinetics and the spatial distribution of the NP growth in the GAS is still missing.

The characterization of the NPs is most easily done when they are collected on solid supports in the deposition chamber. Conventional imaging techniques, such as X-ray diffraction, TEM, and GISAXS[30–32] can be routinely applied to supported NPs to obtain rich information about their size, morphology and structure *in situ* and in real-time during growth. More challenging is the in-flight gas-phase characterization of unsupported NPs. Such measurements may provide an exciting insight into the mechanisms of the NP nucleation, growth and transport undistorted by the interaction with substrates. However, a challenge is often met when one considers that the flux of NPs synthesized by the gas aggregation is not very high and that the in-flight analysis by scattering techniques requires high brilliance synchrotron X-ray sources to obtain an acceptable signal-to-noise ratio. Despite the complexity of the experiments, a few reports are already available that show the successful employment of small-angle X-ray scattering (SAXS) to the *in situ* analysis of the NP formation by flame pyrolysis[41]

[a] Department of Macromolecular Physics, Faculty of Mathematics and Physics, Charles University, V Holesovickach 2, 18000 Prague, Czech Republic
[b] Deutsches Elektronen-Synchrotron (DESY), Notkestr. 85, D-22607 Hamburg, Germany
[c] Chair for Multicomponent Materials, Faculty of Engineering, Kiel University, Kiel, Germany.
[d] KTH Royal Institute of Technology, Department of Fibre and Polymer Technology, Teknikringen 56-58, SE-100 44 Stockholm, Sweden.

Electronic Supplementary Information (ESI) available: Details on the construction of the gas aggregation cluster source and its instalment at DESY, procedure for SAXS calibration, details on SAXS background and data acquisition, procedure for fitting the scattering curves, details of time-resolved measurements, calculation of NP drift velocity.

and by microwave plasma.[42] Recently, X-ray scattering has been also applied for the in-flight characterization of three-dimensional architecture of individual silver NPs on their exit from a magnetron-based GAS.[43] However, the processes of NP formation and growth *inside* a GAS have never been assessed by in-flight imaging techniques, although indirect analyses by Langmuir probe measurements have recently been reported.[44,45] In this work, we aimed at the SAXS analysis of the formation and growth of copper NPs inside a GAS *in situ*, both in close vicinity and at remote distances from the magnetron.

Results and discussion

Synthesis and detection of Cu NPs

A home-built GAS was constructed to allow arbitrary sampling positions within the interior of the aggregation chamber by an X-ray beam (Scheme 1, for the experimental details see ESI).

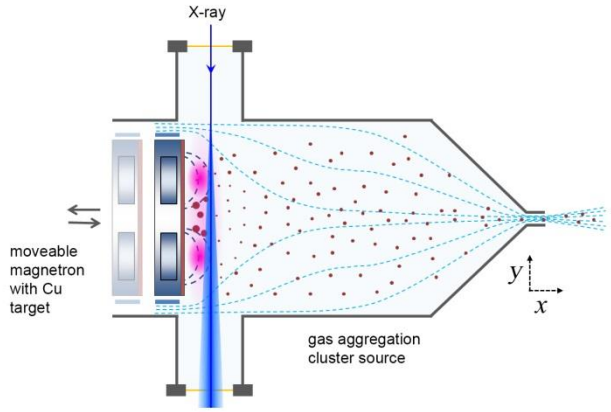

Scheme 1 Experimental arrangement for *in situ* X-ray scattering measurements. SAXS sampling is performed at different axial positions x by moving the magnetron along the GAS and at different radial positions y by moving the entire assembly of the GAS with respect to the X-ray beam in direction normal to the Scheme plane. Dashed dark blue lines indicate the configuration of the magnetic field; light blue dotted lines indicate the hypothetical streamlines of the buffer gas.

The GAS consisted of a cylindrical vacuum chamber with water-cooled walls and was equipped with a moveable 3-inch magnetron and a copper target (HVM Plasma Ltd, 99.99 % purity). Permanent magnets were placed into the magnetron to create a circular plasma ring with a radius of 20 mm above the target. The GAS was connected to the main deposition chamber and the entire assembly was installed at the P03 beamline of PETRA III, DESY, Hamburg, Germany.[46] An elliptically microfocused X-ray beam (22.0 × 32.0 ± 0.5 µm, V × H axes) with the photon energy of 13.01 keV was allowed to pass through the transversal ports of the GAS and to reach a Pilatus 1M detector (Dectris Ltd.; pixel size 172 µm) placed at a distance of 5696 ± 0.5 mm from the axis of the GAS chamber. The largest part of the X-ray flight path outside the GAS was also evacuated, with less than 100 mm being in ambient atmosphere. The setup allowed sampling the inner volume of the GAS within the range of x = 0 − 40 mm and y = ± 12 mm, where x is the axial distance from the magnetron and y is the radial distance measured from the magnetron axis (Scheme 1). The GAS was operated at the Ar pressure of 86 Pa and the flow of 25 sccm. The magnetron was run at DC and voltage set at 500 mA and 320 V, respectively. For more experimental details see also ESI.

For each of the spatial position (x, y) inside the GAS, the scattering images were obtained and processed using the software DPDAK, a customizable code for the analysis of large SAXS data,[47] as described in ESI. The examples of the resultant scattering curves are shown in Figure 1. Here, average integrated scattered intensity I *vs*. scattering wave vector q curves represent the scattering patterns obtained within the GAS at different distances from the magnetron target along its axis at y = 0.0 mm or at different radial distances from the magnetron centre at constant x = 5.0 mm. For the axial dependence, the overall intensity is minimal for the small and large distance from the magnetron while reaching higher values for the intermediate distances. For the radial dependence, the overall intensity decreases slightly from the centre of the magnetron towards the plasma ring.

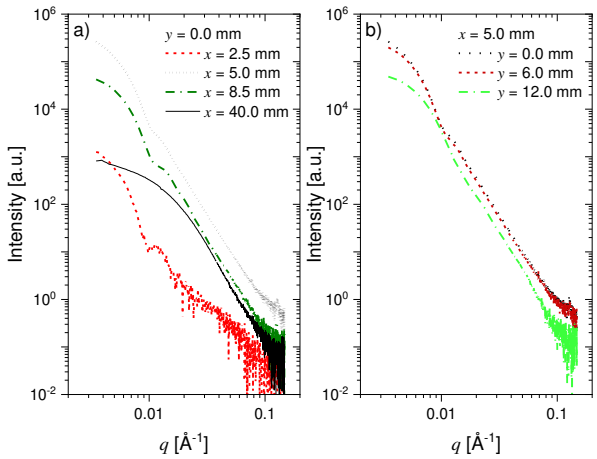

Figure 1 Examples of X-ray scattering curves with subtracted background: a) at different axial distances x from the magnetron target and at the radial distance of y = 0.0 mm (on the GAS axis); b) at different radial distances and at the axial distance of x = 5.0 mm.

NP size and number

All the scattering curves were fitted with a full sphere model with lognormal size distribution, as implemented in the SASView software package[48] to obtain the average NP diameter and the relative volume fraction (i.e. the ratio of the volume occupied by all the NPs to the sampled volume defined by the beam size) for each of the spatial positions (x, y) (for details see ESI). The resultant axial and radial dependences of these parameters are shown in Figure 2 and Figure 3.

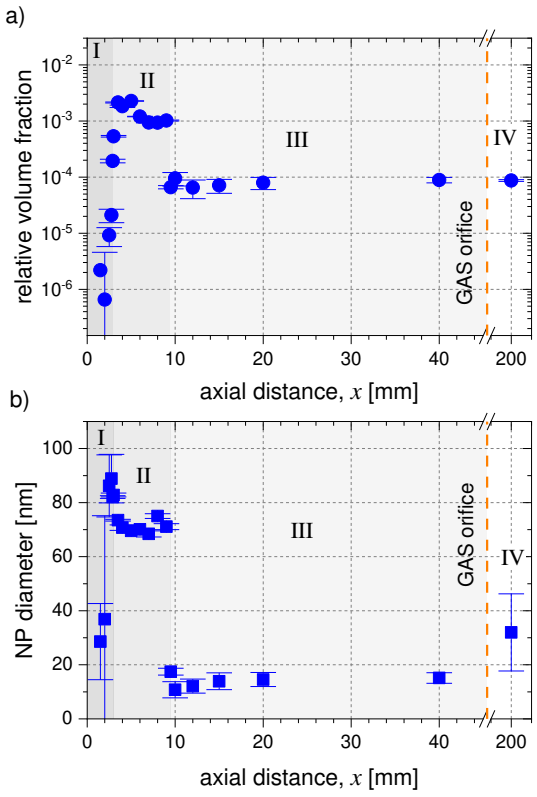

Figure 2 Cu NP parameters in dependence on the axial distance in the GAS: a) relative volume fraction; b) diameter at the radial distance fixed at y = 0.0 mm. The x = 0.0 mm corresponds to the surface of the target. The vertical dotted line designates the position of the exit orifice of the GAS at x = 120.0 mm. Error bars are standard deviation of the NP relative volume fraction and the NP diameter obtained from fitting of 16 individual scattering curves at each spatial position. Roman numerals in differently shaded areas designate different NP growth zones: I – nucleation and growth, II – trapping in the capture zone, III – transport of small NPs along the GAS, IV – transport of small NPs outside the GAS.

A three-order of magnitude increase of the relative volume fraction of the NPs is detected over the distance of 1.5 – 3.0 mm from the magneton target plane (Figure 2a). Even at the smallest accessible distance of 1.5 mm, NPs with an average size of 30 nm are already detected (Figure 2b). We attribute these phenomena to the nucleation and growth of the NPs *via* the attachment of Cu atoms from the gas phase, and designate this region as zone I.

In the further region of 3.0 – 10.0 mm, the NP relative volume fraction and the average size reach maxima and then remain approximately constant. The stability of these parameters indicates that either the nucleation of new NPs is ineffective in this region or the formation of newly-developed NPs is counter-balanced by the NP loss. We designate this region as zone II.

In the next region (zone III), the NP volume fraction steeply decreases by an order of magnitude and then reaches a plateau. The average NP size also decreases to 10 - 15 nm and then stays constant. We attribute the scattering signal in this zone to the NPs that manage to leave the zone II and travel along the GAS. Zone III spreads from 10.0 to 120.0 mm where the exit orifice of the GAS is located.

Finally, zone IV is attributed to the region outside the GAS. Here, the SAXS was measured on the NP beam that exits from the GAS orifice. The average NP size of 32 ± 14 nm was obtained here which exceeds the values determined for zone III inside the GAS. Given that the measurement error is large at x = 200.0 mm, we are presently inclined to think that the discrepancy between the NP size inside and outside the GAS is given by an artefact of the measurement and not by the growth of the NPs within the orifice region. This line of argument is further supported by the fact that the relative volume fraction of the NPs remains markedly constant when moving from zone III to zone IV.

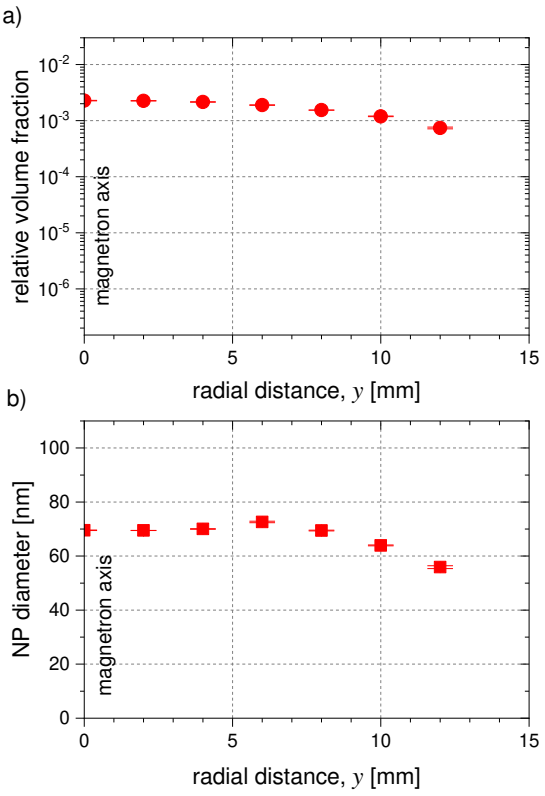

Figure 3 Cu NP parameters in dependence on the radial distance in the GAS: a) relative volume fraction; b) diameter at the axial distance fixed at x = 5.0 mm (zone II). The value of y = 0.0 mm corresponds to the centre of the target. The plasma torus was not accessed (located at y = 20.0 mm, see also Figure S1 of ESI). Error bars are smaller than the symbol size.

The axial distance of x = 5.0 mm was chosen at which the scattering intensity was close to its maximum, and the sampling was performed in the radial direction (Figure 3a and b). An almost constant NP relative volume fraction was detected in the proximity of the axis, decreasing towards the region of the plasma ring around y = 20.0 mm. The position of the plasma torus itself was not accessed in this experimental arrangement. Nevertheless, it is worth noting that the zone closer to the plasma torus is characterized by a less intensive

scattering signal despite the fact that a more intensive sputtering takes place here. The radial dependence of the average NP size evidences that larger NPs become preferentially localized in the central region of the magnetron whereas smaller NPs are detected in the outlying areas.

Identification of different NP growth zones

Taken together, the dependences in Figure 2 and Figure 3 indicate that magnetron sputtering of copper leads to the nucleation and growth of the Cu NPs very close to the target plane in zone I (Scheme 2).

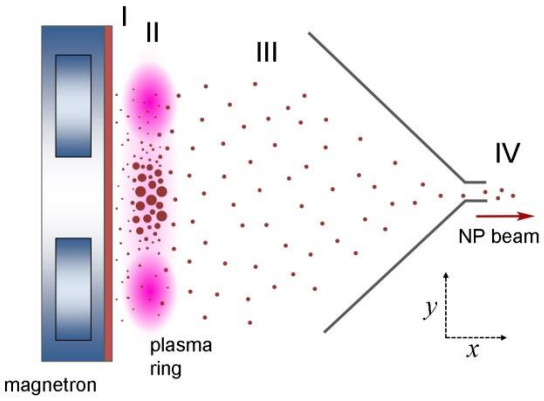

Scheme 2 Different zones of the NP growth: I – nucleation and growth, II – trapping in the capture zone, III – transport of small NPs along the GAS, IV – transport of small NPs outside the GAS.

The NPs preferentially accumulate in the central region which occupies the volume limited by the axial distance of 3.0 – 10.0 mm and by the inner circumference of the plasma torus. The most abundant cloud of the NPs is trapped in this region, which is part of zone II. In order to analyse the size distribution, we opted for the simplest model of a monomodal log distribution. Therefore, we evidently neglect potential inhomogeneity in the size distribution due to the contribution by smaller NPs from the region of the plasma ring as well as by bigger NPs from the central region (for details see ESI). A certain amount of smaller NPs escape zone II and travel through zone III out of the GAS and into the deposition chamber (zone IV).

SEM analysis was used to study the NPs collected on Si support in the deposition chamber at x = 200.0 mm (Figure 4a, b). The NPs produce a circular deposit on the substrate, its thickness being larger in the centre (Figure 4c). Number and volume fraction distributions were calculated from the SEM images and the results are shown in Figure 4d. Note a reasonable agreement between the average size of 27 ± 8 nm of the NPs observed by SEM, and the average size of 32 ± 14 nm obtained from the corresponding fitting of the scattering curves using SASView. Moreover, the SEM images corroborate our approach of a monomodal, but broad size distribution.

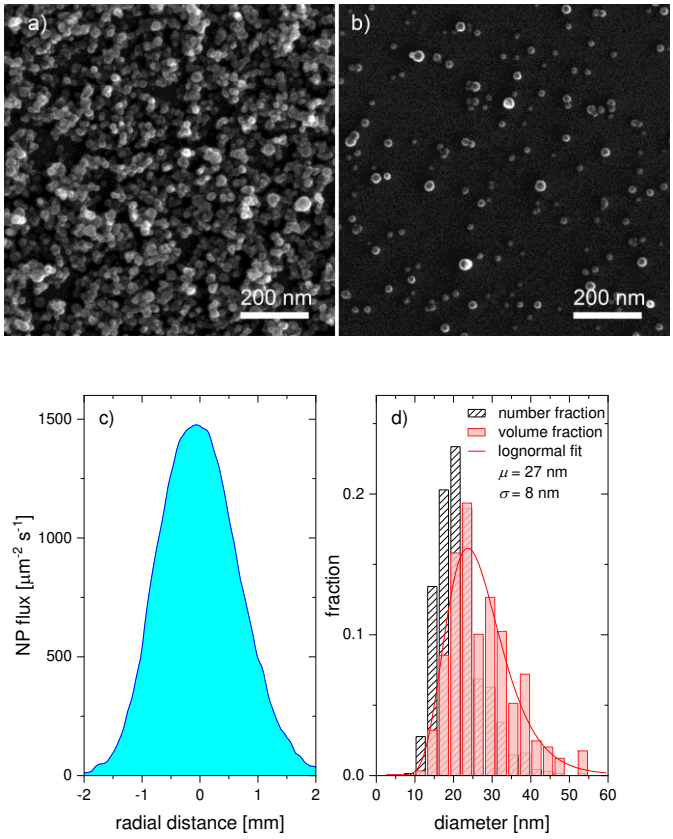

Figure 4 *Ex situ* characterization of Cu NPs. The NPs are collected on Si substrates in the deposition chamber at x = 200.0 mm (zone IV) and with the deposition time of 1 s: a) SEM images are taken in the centre (radial distance is 0 mm) and b) on the periphery (radial distance is 2 mm) of the deposit; c) radial profile of the NP flux calculated from the SEM images of the circular NP deposit; d) number and volume distribution of the NP size calculated from the SEM images as well as the lognormal fit to the volume fraction histogram (average NP diameter is μ = 27 nm, standard deviation σ = 8 nm).

Collapse of the cloud of captured NPs

It is known that NPs acquire an electric charge when immersed or created in the low-temperature plasma, and they can be therefore influenced by the electric field.[49] Apart from the electrostatic force, the NPs experience other forces including gravitation, the ion drag, the neutral drag and the thermophoretic force.[50] The balance between these forces determines the spatial and temporal aspects of the NP distribution in the plasma. We attribute the confinement of the Cu NPs in zone II to the action of the electrostatic force. Our recent findings showed that the spatial profile of the electric field near the magnetron is influenced by the presence of NPs and that localized regions with relatively steep gradients of the plasma potential corresponding to the observed trapping region can appear.[45] We were also able to estimate that 70 – 90 nm NPs can acquire a negative charge of the order of 10^2 elementary charges per particle.[51] The corresponding electric field provides a force sufficient to

balance all other forces acting on the NPs, thus localizing them in the central region of the magnetron and several mm above the target.

To demonstrate this, time-resolved experiments have been performed. The discharge was repeatedly run for 9 s followed by the 6 s off-time, giving the pulse period of 15 s. The scattering intensity was measured along the axis of the aggregation chamber (y = 0.0 mm) at different positions from the magnetron target. This yielded an integrated value of the scattered intensity as discussed in the ESI.

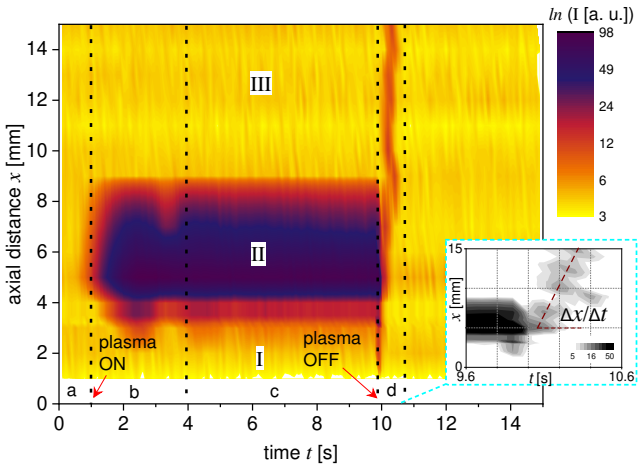

Figure 5 Time-resolved X-ray scattering intensity. The intensity is measured along the x-axis of the aggregation chamber (for details see ESI). Roman numerals designate different NP growth zones as discussed above in the text and shown in Figure 3: I – nucleation and growth, II – trapping in the capture zone, III – transport of small NPs along the GAS. Different temporal stages of the GAS operation are designated as: a) the discharge is off; b) the discharge is turned on at t = 1 s and then it stabilizes at t = 4 s; c) the discharge runs with a stable production of the NPs until it is turned off at t = 10 s; d) the discharge is off and the NPs propagate from the capture zone II towards the exit orifice. The inset shows the d) stage magnified to demonstrate the calculation of the velocity of the NP propagation $\Delta x/\Delta t$.

Figure 5 shows the contour plot of the integrated scattered intensity obtained at different stages of the GAS operation and at different axial distances, in which the intensity is represented by the colour palette from yellow (the lowest intensity) to violet (the highest intensity). The formation of the NPs is detected soon after turning the discharge on at t = 1 s. Again, the scattering intensity is found to be localized at the 3 – 8 mm distance from the magnetron, which confirms the preferential confinement of the NPs in this region. At t = 10 s, the discharge is turned off and the scattering pattern immediately propagates to farther distances from the magnetron target. The phenomenon can be explained by the change in the overall balance of forces acting on the NPs after the switching-off of the discharge. The electric forces cease their action, the neutral drag force prevails and the NPs are removed from the near-to-magnetron region within tenths of a second. The velocity of the NP propagation can be calculated from the slope of the propagating signal after the discharge is turned off (see the inset of Figure 5). The calculated value of $\Delta x/\Delta t$ = 0.04 m/s is comparable (although slightly smaller) to the linear velocity of the Ar flow v = 0.06 m/s (see ESI for details). Pulsing of the discharge can be thus used for the manipulation with confined NPs.

Conclusions

We demonstrated that *in situ* SAXS measurements prove to be a powerful tool for understanding the NP formation, growth and transport in magnetron-based discharges. Complex spatial distribution of the Cu NPs was revealed, with a larger amount of larger (70-90 nm) NPs accumulating preferentially in the near-to-magnetron cloud. Such trapping of NPs within the cluster source has not been considered before. The smaller NPs (10-20 nm) can escape the cloud and are actually those that primarily deposit on substrates. The influence of the electric field on charged NPs is suggested to explain the trapping of the NPs in the vicinity of the magnetron and their drift with the velocity of the carrier gas when the discharge is switched off. Thus, pulsing of the discharge can be suggested as an effective approach to control the NP formation and transport, and to potentially enhance the deposition rate. These findings may be crucial for understanding the phase separation phenomena occurring during the synthesis of complex NPs either from composite targets or by multi-magnetron sputtering.

We emphasize that the results reported herein apply to a particular design of the gas aggregation source and to a particular set of the experimental conditions. It can be anticipated that they can differ significantly for other types of magnetrons, geometry of the aggregation chamber, the gas pressure and flow, the type of metal sputtered etc. Nevertheless, we believe this study opens up a scientific fundament to investigate directly the impact of process conditions and different material composition on NP growth in GAS.

Experimental

Experimental details as well as details on the data acquisition and processing are given in ESI.

Conflicts of interest

There are no conflicts to declare.

Acknowledgements

This work was supported by grant GACR 13-09853S from the Grant Agency of the Czech Republic. M. V., D. N., P. P. also appreciate the support from the student grant SVV 260444/2018 of Charles University. This research was carried out at the synchrotron light source PETRA III at DESY, a member of the Helmholtz Association (HGF).

References

1 A. H. Pfund, *Rev. Sci. Instrum.*, 1930, **1**, 397–399.

2 H. Haberland, M. Karrais and M. Mall, *Zeitschrift fur Phys. D Atoms, Mol. Clust.*, 1991, **20**, 413–415.

3 H. Haberland, M. Karrais, M. Mall and Y. Thurner, *J. Vac. Sci. Technol. A Vacuum, Surfaces, Film.*, 1992, **10**, 3266–3271.

4 S. Pratontep, S. J. Carroll, C. Xirouchaki, M. Streun and R. E. Palmer, *Rev. Sci. Instrum.*, 2005, **76**, 045103.

5 A. Majumdar, M. Ganeva, D. Köpp, D. Datta, P. Mishra, S. Bhattacharayya, D. Ghose and R. Hippler, *Vacuum*, 2008, **83**, 719–723.

6 S. Kumar, T. Pavloudis, V. Singh, H. Nguyen, S. Steinhauer, C. Pursell, B. Clemens, J. Kioseoglou, P. Grammatikopoulos and M. Sowwan, *Adv. Energy Mater.*, 2018, **8**, 1701326.

7 D. M. Foster, R. Ferrando and R. E. Palmer, *Nat. Commun.*, 2018, **9**, 1323.

8 M. Drabik, A. Choukourov, A. Artemenko, O. Polonskyi, O. Kylian, J. Kousal, L. Nichtova, V. Cimrova, D. Slavinska and H. Biederman, *J. Phys. Chem. C*, 2011, **115**, 20937–20944.

9 O. Kylián, V. Valeš, O. Polonskyi, J. Pešička, J. Čechvala, P. Solař, A. Choukourov, D. Slavínská and H. Biederman, *Mater. Lett.*, 2012, **79**, 229–231.

10 G. Kwon, G. A. Ferguson, C. J. Heard, E. C. Tyo, C. Yin, J. DeBartolo, S. Seifert, R. E. Winans, A. J. Kropf, J. Greeley, R. L. Johnston, L. A. Curtiss, M. J. Pellin and S. Vajda, *ACS Nano*, 2013, **7**, 5808–5817.

11 K. R. Bray, C. Q. Jiao and J. N. DeCerbo, *J. Vac. Sci. Technol. B, Nanotechnol. Microelectron. Mater. Process. Meas. Phenom.*, 2014, **32**, 031805.

12 T. Acsente, R. F. Negrea, L. C. Nistor, C. Logofatu, E. Matei, R. Birjega, C. Grisolia and G. Dinescu, *Eur. Phys. J. D*, 2015, **69**, 161.

13 S. Bartling, C. Yin, I. Barke, K. Oldenburg, H. Hartmann, V. von Oeynhausen, M.-M. Pohl, K. Houben, E. C. Tyo, S. Seifert, P. Lievens, K.-H. Meiwes-Broer and S. Vajda, *ACS Nano*, 2015, **9**, 5984–5998.

14 J. Zhao, E. Baibuz, J. Vernieres, P. Grammatikopoulos, V. Jansson, M. Nagel, S. Steinhauer, M. Sowwan, A. Kuronen, K. Nordlund and F. Djurabekova, *ACS Nano*, 2016, **10**, 4684–4694.

15 Y. Yan, T. Santaniello, L. G. Bettini, C. Minnai, A. Bellacicca, R. Porotti, I. Denti, G. Faraone, M. Merlini, C. Lenardi and P. Milani, *Adv. Mater.*, 2017, **29**, 1606109.

16 B. Balasubramanian, R. Skomski, X. Li, S. R. Valloppilly, J. E. Shield, G. C. Hadjipanayis and D. J. Sellmyer, *Nano Lett.*, 2011, **11**, 1747–1752.

17 D. Belić, R. L. Chantry, Z. Y. Li and S. A. Brown, *Appl. Phys. Lett.*, 2011, **99**, 171914.

18 G. E. Johnson, R. Colby, M. Engelhard, D. Moon and J. Laskin, *Nanoscale*, 2015, **7**, 12379–12391.

19 B. Das, B. Balasubramanian, P. Manchanda, P. Mukherjee, R. Skomski, G. C. Hadjipanayis and D. J. Sellmyer, *Nano Lett.*, 2016, **16**, 1132–1137.

20 A. Vahl, J. Strobel, W. Reichstein, O. Polonskyi, T. Strunskus, L. Kienle and F. Faupel, *Nanotechnology*, 2017, **28**, 175703.

21 M. Bohra, P. Grammatikopoulos, V. Singh, J. Zhao, E. Toulkeridou, S. Steinhauer, J. Kioseoglou, J.-F. Bobo, K. Nordlund, F. Djurabekova and M. Sowwan, *Phys. Rev. Mater.*, 2017, **1**, 066001.

22 G. Khadra, A. Tamion, F. Tournus, O. Boisron, C. Albin and V. Dupuis, *J. Phys. Chem. C*, 2017, **121**, 10713–10718.

23 B. Chen, D. de Wal, G. H. ten Brink, G. Palasantzas and B. J. Kooi, *Cryst. Growth Des.*, 2018, **18**, 1041–1046.

24 E. T. Baxter, M.-A. Ha, A. C. Cass, H. Zhai, A. N. Alexandrova and S. L. Anderson, *J. Phys. Chem. C*, 2018, **122**, 1631–1644.

25 Y. Niu, P. Schlexer, B. Sebok, I. Chorkendorff, G. Pacchioni and R. E. Palmer, *Nanoscale*, 2018, **10**, 2363–2370.

26 F. R. Negreiros, A. Halder, C. Yin, A. Singh, G. Barcaro, L. Sementa, E. C. Tyo, M. J. Pellin, S. Bartling, K.-H. Meiwes-Broer, S. Seifert, P. Sen, S. Nigam, C. Majumder, N. Fukui, H. Yasumatsu, S. Vajda and A. Fortunelli, *Angew. Chemie Int. Ed.*, 2018, **57**, 1209–1213.

27 B. Balasubramanian, K. L. Kraemer, N. A. Reding, R. Skomski, S. Ducharme and D. J. Sellmyer, *ACS Nano*, 2010, **4**, 1893–1900.

28 S. Srivastava, J. P. Thomas, M. A. Rahman, M. Abd-Ellah, M. Mohapatra, D. Pradhan, N. F. Heinig and K. T. Leung, *ACS Nano*, 2014, **8**, 11891–11898.

29 O. Kylián, A. Kuzminova, M. Vaydulych, M. Cieslar, I. Khalakhan, J. Hanuš, A. Choukourov, D. Slavínská and H. Biederman, *Plasma Process. Polym.*, 2018, **15**, 1700109.

30 M. Schwartzkopf, A. Buffet, V. Körstgens, E. Metwalli, K. Schlage, G. Benecke, J. Perlich, M. Rawolle, A. Rothkirch, B. Heidmann, G. Herzog, P. Müller-Buschbaum, R. Röhlsberger, R. Gehrke, N. Stribeck and S. V. Roth, *Nanoscale*, 2013, **5**, 5053.

31 M. Schwartzkopf and S. Roth, *Nanomaterials*, 2016, **6**, 239.

32 M. Schwartzkopf, A. Hinz, O. Polonskyi, T. Strunskus, F. C. Löhrer, V. Körstgens, P. Müller-Buschbaum, F. Faupel and S. V. Roth, *ACS Appl. Mater. Interfaces*, 2017, **9**, 5629–5637.

33 Y.-H. Xu and J.-P. Wang, *Adv. Mater.*, 2008, **20**, 994–999.

34 D. Llamosa, M. Ruano, L. Martínez, A. Mayoral, E. Roman, M. García-Hernández and Y. Huttel, *Nanoscale*, 2014, **6**, 13483–13486.

35 G. E. Johnson, R. Colby and J. Laskin, *Nanoscale*, 2015, **7**, 3491–3503.

36 G. E. Johnson, T. Moser, M. Engelhard, N. D. Browning and J. Laskin, *J. Chem. Phys.*, 2016, **145**, 174701.

37 P. Mukherjee, B. Balamurugan, J. E. Shield and D. J. Sellmyer, *RSC Adv.*, 2016, **6**, 92765–92770.

38 J. Vernieres, S. Steinhauer, J. Zhao, A. Chapelle, P. Menini, N. Dufour, R. E. Diaz, K. Nordlund, F. Djurabekova, P. Grammatikopoulos and M. Sowwan, *Adv. Funct. Mater.*, 2017, **27**, 1605328.

39 P. Solař, O. Polonskyi, A. Olbricht, A. Hinz, A. Shelemin, O. Kylián, A. Choukourov, F. Faupel and H. Biederman, *Sci. Rep.*, 2017, **7**, 8514.

40 J. Hanuš, M. Vaidulych, O. Kylián, A. Choukourov, J. Kousal, I. Khalakhan, M. Cieslar, P. Solař and H. Biederman, *J. Phys.*

D. Appl. Phys., 2017, **50**, 475307.
41 G. Beaucage, H. K. Kammler, R. Mueller, R. Strobel, N. Agashe, S. E. Pratsinis and T. Narayanan, *Nat. Mater.*, 2004, **3**, 370–373.
42 S. Popescu, E. Jerby, Y. Meir, Z. Barkay, D. Ashkenazi, J. B. A. Mitchell, J.-L. Le Garrec and T. Narayanan, *J. Appl. Phys.*, 2015, **118**, 023302.
43 I. Barke, H. Hartmann, D. Rupp, L. Flückiger, M. Sauppe, M. Adolph, S. Schorb, C. Bostedt, R. Treusch, C. Peltz, S. Bartling, T. Fennel, K.-H. Meiwes-Broer and T. Möller, *Nat. Commun.*, 2015, **6**, 6187.
44 M. A. Koten, S. A. Voeller, M. M. Patterson and J. E. Shield, *J. Appl. Phys.*, 2016, **119**, 114306.
45 J. Kousal, A. Kolpaková, A. Shelemin, P. Kudrna, M. Tichý, O. Kylián, J. Hanuš, A. Choukourov and H. Biederman, *Plasma Sources Sci. Technol.*, 2017, **26**, 105003.
46 A. Buffet, A. Rothkirch, R. Döhrmann, V. Körstgens, M. M. Abul Kashem, J. Perlich, G. Herzog, M. Schwartzkopf, R. Gehrke, P. Müller-Buschbaum and S. V. Roth, *J. Synchrotron Radiat.*, 2012, **19**, 647–653.
47 G. Benecke, W. Wagermaier, C. Li, M. Schwartzkopf, G. Flucke, R. Hoerth, I. Zizak, M. Burghammer, E. Metwalli, P. Müller-Buschbaum, M. Trebbin, S. Förster, O. Paris, S. V. Roth and P. Fratzl, *J. Appl. Crystallogr.*, 2014, **47**, 1797–1803.
48 https://www.sasview.org
49 A. Melzer and J. Goree, in *Low Temperature Plasmas: Fundamentals, Technologies and Techniques*, eds. R. Hippler, H. Kersten, M. Schmidt and K. H. Schoenbach, 2008.
50 J. Berndt, E. Kovačević, I. Stefanović, O. Stepanović, S. H. Hong, L. Boufendi and J. Winter, *Contrib. to Plasma Phys.*, 2009, **49**, 107–133.
51 J. Blažek, J. Kousal, H. Biederman, O. Kylián, J. Hanuš and D. Slavínská, *J. Phys. D. Appl. Phys.*, 2015, **48**, 415202.